LETTER

3D woodpile structure tunable plasma photonic crystal

To cite this article: B Wang *et al* 2019 *Plasma Sources Sci. Technol.* **28** 02LT01

View the article online for updates and enhancements.

Letters

Letter

3D woodpile structure tunable plasma photonic crystal

B Wang , J A Rodríguez and M A Cappelli

Department of Mechanical Engineering, Stanford University, Stanford, CA 94305-3032, United States of America

E-mail: cap@stanford.edu

CrossMark

Abstract

A three-dimensional woodpile structure tunable plasma photonic crystal is designed, simulated, and experimentally characterized over the $S–X$ band of the electromagnetic (EM) spectrum. The measurements confirm that the EM response is rich in dynamics. The photonic crystal's reconfigurability achieved through individual discharge control of the properties of the woodpile plasma columns offers an unprecedented opportunity to better resolve the interactions between both the Bragg and localized surface plasmon modes which dominate the spectrum at lower frequencies. Both the experiments and simulations reveal evidence for the coupling of Bragg and surface plasmon modes through a Fano resonance.

Photonic crystals (PCs) are artificially-ordered materials designed to transmit or reflect electromagnetic (EM) waves over a limited range of frequencies as a result of destructive and constructive Bragg scattering interferences within the periodic structure [1]. A plasma photonic crystal (PPC) [2–6] is a PC that uses controllable gaseous plasma elements to offer a degree of tunability or reconfigurability. The simplest PPCs consist of one-dimensional (1D) striated plasma-vacuum or plasma-dielectric layers [2, 7]. The most commonly-studied 1D PPCs are laser-produced plasma Bragg gratings [8, 9]. Two-dimensional (2D) and three-dimensional (3D) PPCs are arrays of stand-alone plasma structures [4, 5] or dielectric/metallic PCs that incorporate repeating plasma structures. As in passive PCs, PPCs can be functionalized by introducing defects that break the crystal periodicity. For example, reconfigurable line defects in a 2D PPC have been shown to result in switchable waveguiding [10]. Theoretical work in PPCs has investigated the unique physics behind these types of devices, including surface modes [11], Bragg scattering [12], and induced transparency [13]. Passive dielectric or metal PCs can also be functionalized by incorporating plasma defects to produce novel devices such as tunable bandpass filters [6] and power limiters [14], and in

some cases, novel resonator cavities as plasma formation devices [15]. Plasmonic effects in PPCs, such as the excitation of bulk or localized (surface) plasmons, can further enhance the EM wave interactions [7, 16], resulting in deep and wide attenuation bands. In 2D PPCs, these plasmonic effects arise for TE polarization of the incident field (E-field $\perp$ to plasma rods) at frequencies below the plasma frequency, ω_p.

In this letter we describe the construction and performance of a 3D PPC consisting of a woodpile lattice structure formed from intertwined orthogonal nested 2D arrays constructed from gaseous plasma columns. The woodpile lattice structure allows for the excitation of both surface plasmon and Bragg scattering modes for arbitrary incident polarization. The plasma column properties, specifically in this device, the plasma density, can be individually controlled allowing reconfigurability of the PC. For example, we can turn off the plasma of all of the columns oriented in one direction, transforming the structure into a lower dimensionality 2D array. As described below, we show that there is a synergistic interaction of the two nested 2D arrays, affected by the excitation of surface plasmon polaritons. We also show that the reconfigurability of the device is tuned by changing
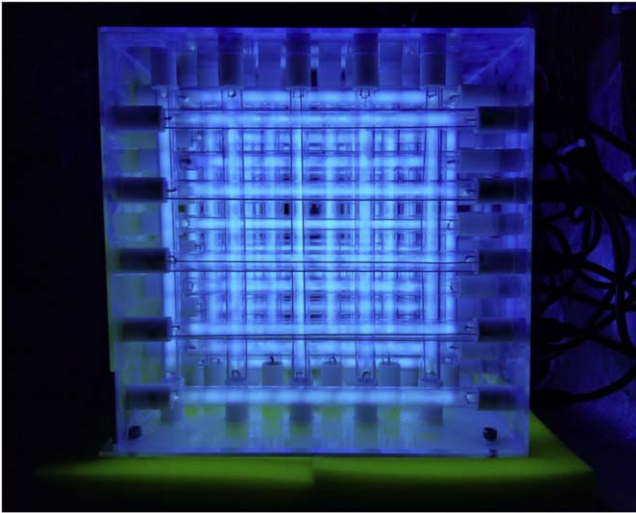
Figure 1. 3D plasma photonic crystal consisting of 50 plasma discharge tubes arranged in a woodpile configuration.

the plasma density of all plasma elements in the 3D crystal, allowing for a dynamically adjustable transmission spectra.

Figure 1 shows a photograph of the 3D PPC woodpile structure consisting of layers of 5×5 parallel electrical plasma discharge tubes with a lattice spacing of $a = 50$ mm. Each neighboring layer is rotated by $90°$ and spaced $a/2 = 25$ mm from the previous layer while offset by $a/2 = 25$ mm to form the woodpile configuration with a total of 10 layers, as illustrated in figure 2. The discharge tubes are

held in place at four of the crystal boundaries by an acrylic scaffold to form the woodpile structure. The individually controllable alternating-current (AC) discharge tubes have a 290 mm long quartz envelope which is 15 mm in outer diameter with a 1 mm wall thickness. The tubes are filled with argon, with added mercury to a pressure of 250 Pa. The gas temperature during nominal operation is approximately 330 K, resulting in a mercury vapor partial pressure of about 3.5 Pa. Each discharge is driven individually by an AC ballast with a peak-to-peak voltage, $V_{pp} = 160$ V. The voltage waveform of each discharge is triangular in shape resulting in a root mean square voltage of $V_{rms} = 80/\sqrt{3}$ V. The ballasts have a variable peak current (also close to triangular) to control the discharge parameters, ranging from 24.8 to 111.1 mA, with a ballast frequency that decreases linearly from 55.0 to 37.0 kHz for increasing peak current in the range from 24.8 to 51.2 mA, and a ballast frequency in the range of 32.2–33.8 kHz for peak discharge currents from 54.4 to 111.2 mA. Based on previous studies [6], where we examined the dependence of the surface plasmon gap on discharge current in a 2D PPC constructed from these discharge tubes, we estimate that the average plasma density within the discharge is $n_e(cm^{-3}) \approx 1.1 \times 10^{10}I_p(mA)$. We note that the required plasma densities needed in the simulations of [5] to predict the observed transmission structure are slightly higher (by a factor of 2) than those inferred from [6], based on the plasma-filled vacancy tuning of an alumina PC. This difference is attributed to the strong dependence of the defect state energy on plasma size and location within the defect, whereas
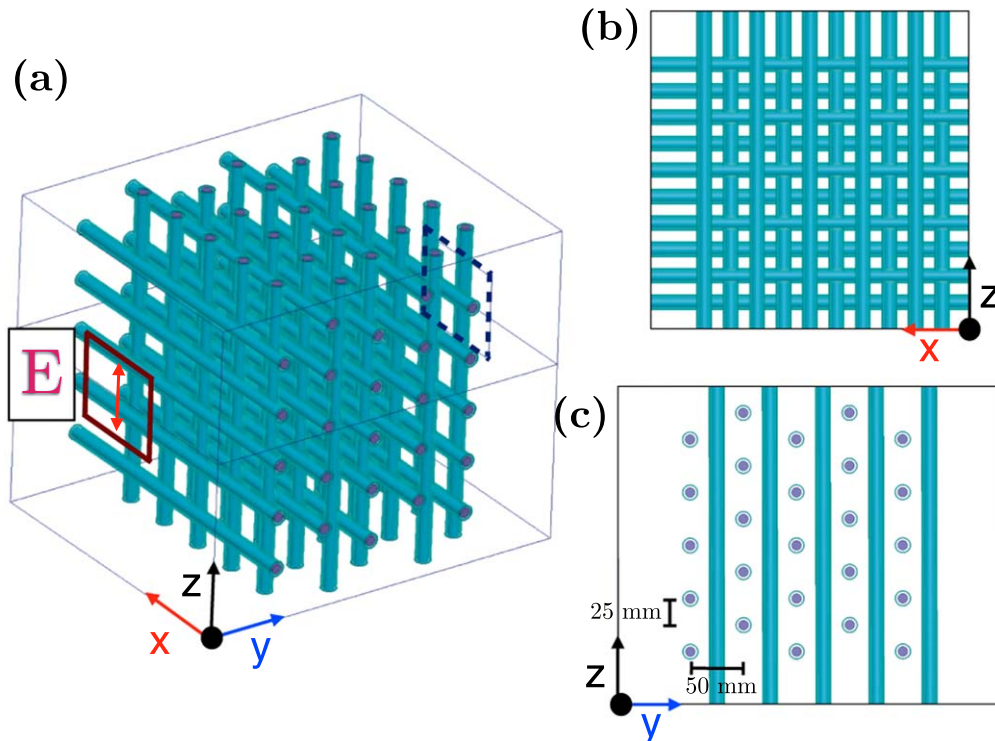
Figure 2. (a) Perspective schematic of the 3D woodpile PPC. The solid red and dashed black rectangles indicate the position of the microwave horn antennas for both the experiments and simulations. (b) x–z view of the woodpile structure showing the 3D lattice structure. The k-vector of the incident wave is in the y-direction. (c) y–z view of the woodpile structure depicting the lattice constant $a = 50$ mm, staggered by $a/2$ (25 mm) in the z-direction for each array element in the y axis. The quartz tubes are represented in teal, while the plasma rods are shown in purple.

the localized surface plasmon (LSP) frequency depends mainly on the plasma density.

We use the ANSYS commercial software package referred to as the high frequency EM field simulator (ANSYS HFSS 16) to compute the EM fields and transmission spectra. The simulations are carried out in 3D. The plasma columns are modeled with a frequency dependent Drude dielectric constant given by

$$\varepsilon_p = 1 - \frac{\omega_p^2}{\omega(\omega + i\nu)}, \quad (1)$$

where ω is the EM wave frequency, ν is the electron collisional damping rate, and ω_p is the plasma frequency, given by $\omega_p = \sqrt{n_e e^2/m_e \varepsilon_o}$ with n_e, e, and m_e the column electron number density, electron charge, and electron mass, respectively, and ε_o is the vacuum permittivity. As described in our prior study [6], to account for the radially non-uniform plasma density we assume in the simulations that the plasma electrons are distributed uniformly over a reduced diameter of 9.2 mm, resulting in a region of electron density that is twice that of the case where the electrons are distributed uniformly over the entire inner tube diameter of $d = 13$ mm. It is noteworthy that surface plasmon modes, and, more specifically, Fano modes (when the surface plasmon frequency coincides with the lattice frequency [16]), have fields that are concentrated closer to the plasma-vacuum interface [17]. As a result, the use of such an average density in the plasma simulations are expected to over predict the surface plasmon-associated shifts. Recently, Thomas *et al* [18] computed the surface plasmon shift and associated Fano resonances for a 2D PPC and confirmed that in addition to a slightly reduced shift, there is also a slight increase in the broadening of the transmission feature in comparison to the uniform profile. The use of a uniform plasma density in the simulations that we carry out for comparison to our experimental measurements does not effect the general conclusions that we arrive at. In these simulations, we also assume a value of $\nu = 1$ GHz for the electron collisional damping rate, as this value resulted in good agreement between the measured and experimental transmission in previous studies [6]. We include the presence of the quartz tube (99.9% purity) with an assumed dielectric constant $\varepsilon = 3.8$. As illustrated in figure 2(a), the source antenna is placed at the the location depicted by the red rectangle with polarization (*E*-field) in the *z*-direction (transverse to the first-layer plasma columns). The receiver antenna is placed at the depicted location of the black dashed-line rectangle on the back side of the PPC. Radiative conditions are imposed on all external boundaries.

In the experiments, a pair of broadband microwave horn antennas (A INFO LB-20180 2 GHz—18 GHz) are used as the source and detector, located in the rectangles shown in figure 2(a), spaced 30 cm apart, also with the *E*-field polarized in the *z*-axis. The antennas are connected to a HP 8722D Vector Network Analyzer to measure the *s*-parameters, particularly S_{21}, which represents the EM transmission through the crystal. The measured transmission reported below was

recorded with an integration time of 5 ms per frequency point in the scan, with a source power set at -5 dBm.

The use of plasmas allows for LSP excitation at the plasma—quartz/air interface at frequencies below the plasma frequency when the *E*-field is in a plane perpendicular to the plasma columns. For 2D PPCs, LSPs are excited for TE polarizations only, with Bragg scattering modes expected for both polarizations. As we show below, this 3D PPC exhibits characteristics attributable to both LSP and Bragg scattering, and the attenuation is not simply the linear combination of that associated with the interwoven 5×5 orthogonal 2D PPCs, but instead, exhibits synergistic effects arising from the interplay between the EM activity contributed by both lattices in this woodpile configuration.

Experimental and simulated transmission spectra are shown in figure 3. With the plasma discharges turned off (figure 3(a)) attenuation is fairly shallow, but there are discernible band gaps attributable to the quartz throughout the spectrum, most notably near 3 GHz, with some correspondence to features in the simulations. With the plasma on and at relatively low discharge currents $I_P = 24.8$ mA (figure 3(b)) and $I_P = 28.0$ mA (figure 3(c)), the refractive index of the plasma is still close to unity and the higher frequency regions of the spectrum show little change in comparison to the plasma off case, indicating that the presence of the plasma has but a small effect on the quartz photonic bands in this region, nor do we see any new plasma-specific bands. However, there is a marked difference at frequencies below the plasma frequency. For example, in figure 3(b), we see the emergence a spectra feature that we attribute to an LSP band at a frequency below the lowest quartz Bragg gap recorded in the experiment. In cylindrical plasma columns, when the incident wavelengths are much larger than the column radius, we expect the LSP resonance to be at approximately $\omega_{LSP} = \frac{\omega_p}{\sqrt{2}}$ [19]. The location of the expected LSP in the figures are based on the approximate relation between n_e and I_p given earlier. The approximate location of the PPC Bragg resonance (BG) identified in the figures is based on the location of the quartz gap, as there is no definitive means of isolating that gap from the effect of the LSP feature. At the slightly higher discharge current (figure 3(c)), the LSP resonance may be nearly coincident with the PPC Bragg gap and a complex spectrum emerges, suggestive of a lattice (Fano) resonance [16], with a second peak emerging near 4 GHz. The simulated spectra for these intermediate discharge current cases ($n_e = 2 \times 10^{11}$ cm^{-3}, or $\omega_p = 4$ GHz and $n_e = 3.8 \times 10^{11}$ cm^{-3}, or $\omega_p = 5.5$ GHz, respectively) capture the experimental spectra reasonably well, most notably, the emergence of a second peak (in figure 3(c)) which may be due to the spectral splitting of coincident coupled resonators generally seen in Fano resonances. At the highest current density case (figure 3(d)), this coupled resonance is quite pronounced as indicated by the depth of the attenuation and a splitting of the measured spectrum. For comparison, we include a simulated spectrum for a plasma frequency $\omega_p = 7$ GHz ($n_e = 6 \times 10^{11}$ cm^{-3}), although it is apparent that the predicted spectrum has the
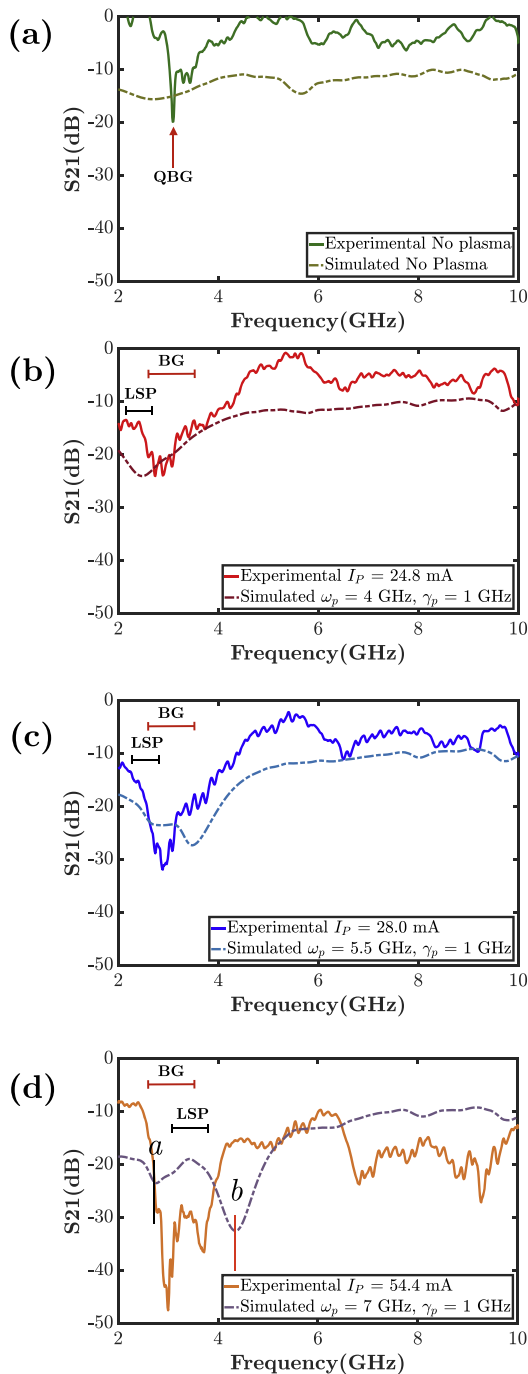
Figure 3. Experimental and simulated transmission (S_{21}) through the 3D woodpile plasma photonic crystal. (a) Plasma off, and only quartz tubes. The quartz bandgap (QBG) is due to the photonic crystal structure of the quartz envelopes. (b) Plasma on with discharge current $I_P = 24.8$ mA, simulated $\omega_p = 4$ GHz, $\gamma_p = 1$ GHz. The localized surface plasmon (LSP) and the Bragg gap (BG) begin appearing at this plasma density. (c) Plasma on with discharge current $I_P = 28.0$ mA, simulated $\omega_p = 5.5$ GHz, $\gamma_p = 1$ GHz. The LSP shifts upwards in frequency and begins merging with the BG. (d) Plasma on with discharge current $I_P = 54.4$ mA, simulated $\omega_p = 7$ GHz, $\gamma_p = 1$ GHz. At this plasma frequency, the LSP shifts above the BG frequency and causes a splitting to occur, leading to two adjacent gaps and a small transmission band within the bandgaps.
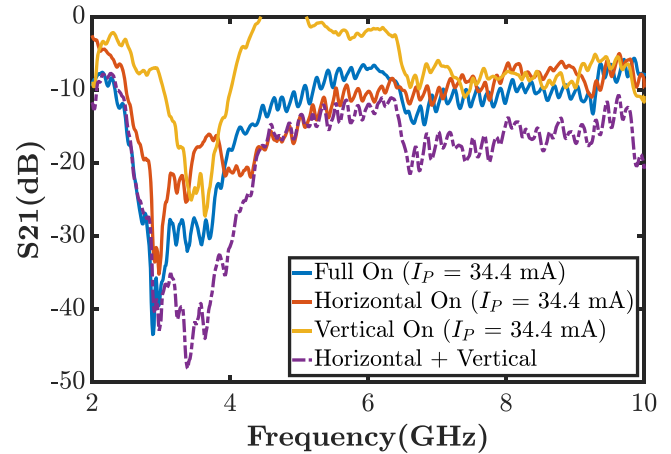
Figure 4. Experimental transmission (S_{21}) through the 3D woodpile plasma photonic crystal for all plasma columns turned on, horizontal (x-aligned) plasmas turned on, vertical (z-aligned) plasmas turned on, and sum of horizontal and vertical on tube configurations with discharge current $I_P = 34.4$ mA. There is a clear interaction between the horizontal and vertical plasma columns when both are on, as the transmission of the sum of the two do not result in the transmission arising when both are active.
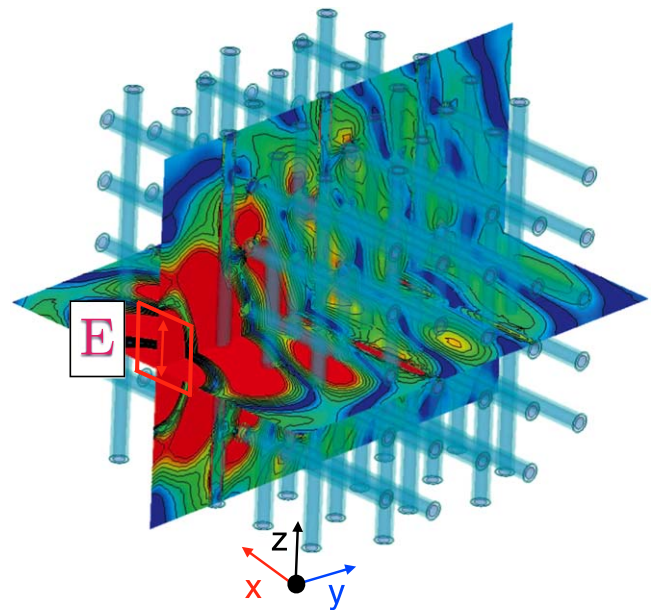
Figure 5. Simulated E-fields (magnitude) for the 3D woodpile photonic crystal with $\omega_p = 7$ GHz, $\gamma_p = 1$ GHz at $f = 2.775$ GHz. The fields are shown for the $y{-}z$ and $y{-}x$ planes passing through the center of the PPC primarily to orient the reader in the interpretation of the field maps and field vectors shown in figure 6. The strong field attenuation for the highest plasma density case is clearly indicated when the incident fields are tuned to the frequency associated with the peak in the attenuation seen in figure 3(d).

peak frequencies further apart than what is measured, in part due to an assumed plasma density that is perhaps larger than in the experiments. The shifted experimental transmission spectra compared to simulations in this region of the spectrum is not surprising, as the simulations are highly idealized with the assumption of uniform plasma columns separated from the quartz wall by vacuum. More surprising is that for this
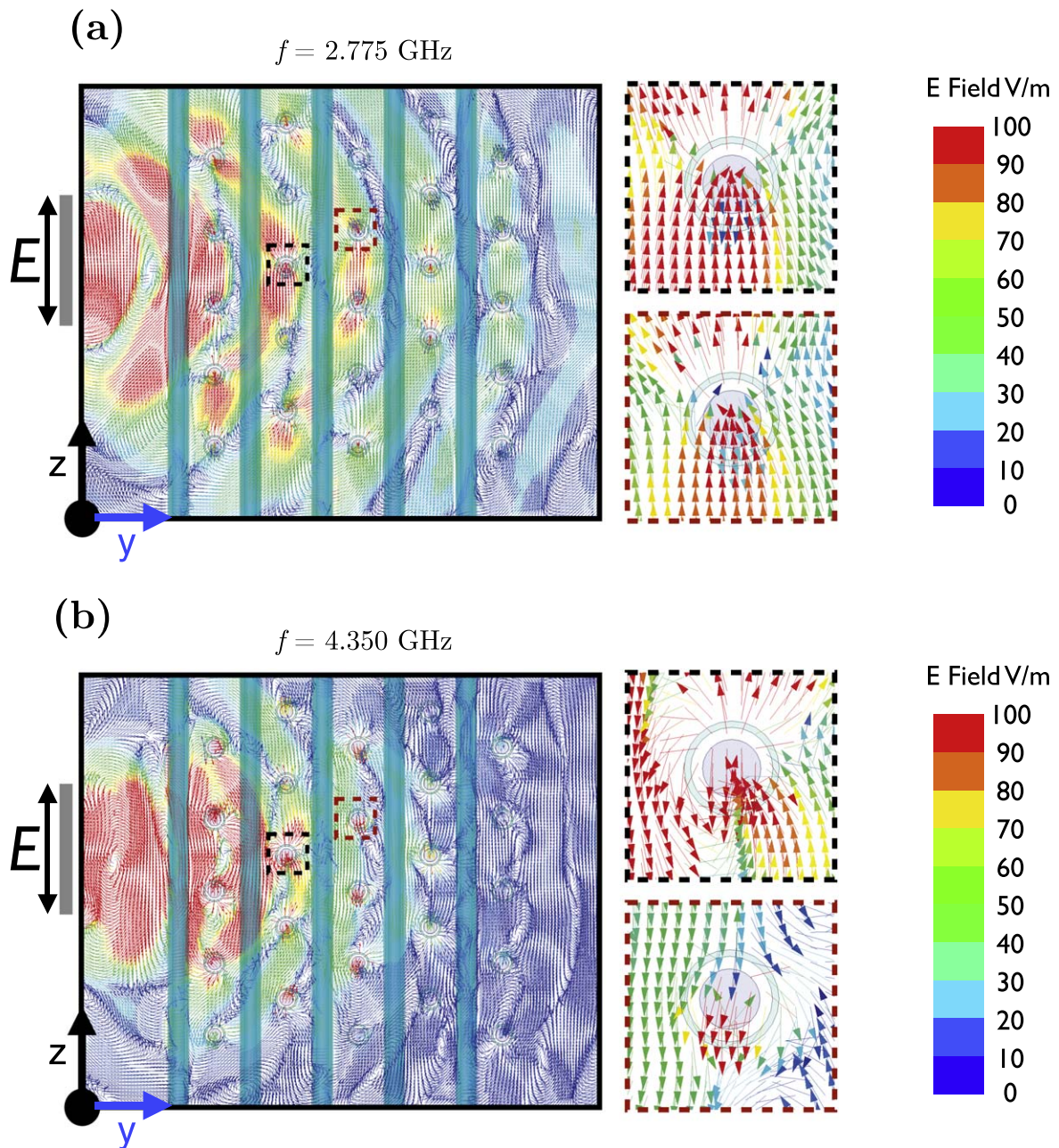
Figure 6. Simulated y–z cross section E vector field for the 3D woodpile photonic crystal with $\omega_p = 7$ GHz, $\gamma_p = 1$ GHz at (a) $f = 2.775$ GHz (b) $f = 4.350$ GHz. The vector fields reveal the presence of surface plasmon modes around the plasma discharge at specified frequencies and the possible coupling between neighboring plasma elements.

higher current density case, we see the emergence of fairly strong features that are not captured in the HFSS simulations. These features are primarily associated with the response of the E-field aligned plasma columns and are due to higher frequency Bragg gaps and not the excitation of surface plasmons. The lack of these associated high frequency Bragg structures are a consequence of how the HFSS simulations launch and receive the EM waves. Modeling the actual acceptance aperture and gain of the real antennas is complex, as this varies strongly with frequency. A limited number of simulations carried out using finite difference time domain (FDTD) simulations do a better job at resolving this higher

frequency range, and confirms the presence of this structure seen experimentally.

We plot the transmitted spectra for a discharge current of $I_P = 34.4$ mA in figure 4. Here we highlight three cases: (a) the case where the PPC is completely activated (the horizontal, or x-aligned and vertical, or z-aligned plasma tubes in figure 2(a)); (b) only the horizontal tubes are active; and (c) only the vertical tubes are active. For comparison to case (a), we also plot the linear sum of the transmission of (b) and (c). When only the vertical (z-aligned) tubes are active we do not expect LSP excitation. The single attenuation band seen at low frequencies near 3.5 GHz is therefore the Bragg gap of the 2D hexagonal array with TM polarization. There appear to

be weak Bragg gaps at frequencies >6 GHz. For this vertical tube only case, there appears to be relatively strong structure at frequencies >6 GHz which is due to Bragg scattering, as this configuration eliminates the possibility of exciting localized plasmon modes. As mentioned earlier, this structure is not as strong in the HFSS simulations due to the simplified treatment of the antennas, although we have confirmed its presence in FDTD simulations. When only the horizontal (*x*-aligned) tubes are active we see a split spectrum at low frequency for the 2D array with TE polarization, suggesting coupled LSP and BGs. There are no discernible features at high frequencies. At frequencies above 3 GHz, the sum of the transmission measured for the individual 2D PPCs is much less than that measured when all plasma columns are ignited indicating that there is synergistic destructive interference between the two nested 2D arrays. Below 3 GHz, it seems that a linear summation captures the measured spectrum well, which is dominated by the 2D array with TE excitation, likely as a result of a strong LSP attenuation. At high frequencies, the attenuation is dominated by the 2D (TM) array, but the measured attenuation is still less than that predicted by the linear summation of the individual spectra.

Some insight is gained from the simulations, particularly at lower frequencies, by examining the behavior of the predicted electric fields. To orient the reader, a 3D schematic of the PPC with superimposed E-field magnitudes (at an instant in time) is shown in figure 5 for $\omega_p = 7$ GHz, $\gamma_p = 1$ GHz at $f = 2.775$ GHz. The fields are shown for the *y–z* and *y–x* planes passing through the center of the PPC. The *y–z* plane in figure 5 is the plane where the vector E-field is displayed in figure 6. In figure 6(a), the vector fields are shown for the low frequency feature labeled as 'a' in figure 3(d), i.e. $f = 2.775$ GHz. The attenuation of the incident fields confirm the presence of Bragg interferences, and E-field phase sweeps of the region incident on two of the plasma columns with axes $\perp E$ (red and black dashed boxes) indicate the excitation of LSPs that are in phase with the incident Bragg fields. A close-up of these regions confirm that these are surface plasmons, with local E-fields that are amplified to levels above that of the background. At $f = 4.35$ GHz (figure 6(b)), corresponding to the higher frequency feature in figure 3(d), again we see Bragg attenuation, and the LSPs around the same two plasma columns are even more pronounced. The presence of the LSPs at two nearby frequencies where there appear to be strong Bragg gap attenuations and the phase synchronization in time are consistent with a lattice or Fano resonance. Not apparent in these figures but evident in the simulated E-field phase sweeps are suggestions that the incident Bragg fields also couple into longitudinal surface plasmon waves that propagate along the *z*-aligned plasma columns.

The measurements and simulations described here, of a 3D PPC with a woodpile configuration, present an EM system that is rich in dynamics and an opportunity for reconfigurability that is not generally found in microwave PCs. We see compelling evidence for the coupling of Bragg and LSP modes through a Fano resonance. The design allows for individual control of each element in the 3D crystal. Future research will examine the propagation of waves along complex defects (associated with non-activated plasma elements) that extend in three dimensions. The 3D crystal provides the framework for the design of novel 3D PC devices such as 3D cloaking, 3D resonators and field localization, and temporally variable 4D devices.

Acknowledgments

ORCID iDs

B Wang ● https://orcid.org/0000-0002-7192-4249
J A Rodríguez ● https://orcid.org/0000-0001-7892-6207
M A Cappelli ● https://orcid.org/0000-0003-3093-3357

References

[1] Joannopoulos J J D, Johnson S, Winn J N J and Meade R R D 2008 *Photonic Crystals: Molding the Flow of Light* 2nd edn (Princeton, NJ: Princeton University Press)
[2] Hitoshi H and Mase A 2004 *J. Plasma Fusion Res.* **80** 89–90
[3] Sakai O and Tachibana K 2012 *Plasma Sources Sci. Technol.* **21** 013001
[4] Sakai O, Sakaguchi T and Tachibana K 2007 *J. Appl. Phys.* **101** 073305
[5] Wang B and Cappelli M A 2016 *Appl. Phys. Lett.* **108** 161101
[6] Wang B and Cappelli M A 2015 *Appl. Phys. Lett.* **107** 171107
[7] Wang B, Righetti F and Cappelli M 2018 *Phys. Plasmas* **25** 031902
[8] Shi L *et al* 2011 *Phys. Rev. Lett.* **107** 095004
[9] Liu F *et al* 2017 *Opt. Express* **25** 22303–11
[10] Wang B and Cappelli M A 2016 *AIP Adv.* **6** 065015
[11] Shukla S, Prasad S and Singh V 2015 *Phys. Plasmas* **22** 092111
[12] Qi L, Li C, Fang G and Gao X 2015 *Plasma Sci. Technol.* **17** 4–9
[13] Scalora M, Bloemer M J, Pethel A S, Dowling J P, Bowden C M and Manka A S 1998 *J. Appl. Phys.* **83** 2377
[14] Gregório J, Parsons S and Hopwood J 2017 *Plasma Sources Sci. Technol.* **26** 055002
[15] Parsons S and Hopwood J 2017 *IEEE Electron Device Lett.* **38** 1602–5
[16] Righetti F, Wang B and Cappelli M 2018 *Phys. Plasma* **25** 124502
[17] Tan H, Jin C, Zhuge L and Wu X 2018 *IEEE Trans. Plasma Sci.* **46** 539–44
[18] Thomas W, Shumlak U and Righetti F 2018 *60th Annual Meeting of the APS Division of Plasma Physics* vol 60, PP 11.118 http://meetings.aps.org/Meeting/DPP18/Session/
[19] Pitarke J, Silkin V, Chulkov E and Echenique P 2006 *Rep. Prog. Phys.* **70** 1